European Rotorcraft Forum

Experimental test-bed for the identification of biodynamic feedthrough of helicopter-pilot systems

A. Zanoni*,◇, D. Marchesoli◇, C. Talamo◇, P. Masarati◇
F. Colombo†, S. Kemp‡, E. Fosco†

◇Politecnico di Milano - Dipartimento di Scienze e Tecnologie Aerospaziali, Campus Bovisa, Via La Masa 34, 20156 Milano, Italy
†Leonardo Helicopters Division, Cascina Costa di Samarate (VA), Italy
‡Leonardo Helicopters Division, Lysander Rd, Yeovil BA20 2YB, UK

* e-mail: andrea.zanoni@polimi.it

Abstract

The design of rotorcraft, especially when the human-machine interaction is concerned, has to take into account the possible interactions between the pilot biomechanics and the rotorcraft dynamics. To this end, existing and novel design techniques and procedures geared toward robust prevention of Rotorcraft-Pilot Couplings need experimental validation to enable their effective application by OEMs. For this purpose, an experimental test bench, providing means to measure the biodynamic feedthrough of pilot-rotorcraft systems is presented. The system has been designed to be easily reconfigurable in order to represent different cockpit designs. Results obtained with a professional test pilot on two different cockpit layouts are presented. The identified biodynamic feedthrough transfer functions are then exploited along with a simplified representation of the helicopter heave dynamics to perform stability assessments regarding the collective bounce phenomenon.

1 Introduction

Demands to the design process of aircraft, particularly of rotorcraft, have been ever-increasing in the last few years. One important aspect that has to be considered carefully in the early design process is the pilot-vehicle interactional dynamics, generally referred to under the name of Rotorcraft-Pilot-Couplings (RPC), that can be at the root of different kinds of unwanted feedback loops:

- PIO (Pilot-Induced Oscillations);
- PAO (Pilot-Assisted Oscillations).

While the former attracted the vast majority of the research focus in the last six decades, starting from the seminal work of Ashkenas et al [1] in 1964, through the profound refactoring introduced by McRuer in the 1990s [2,3] through modern-day activities [4–10]; the second kind, involving vibration feedback loops between the rotorcraft structural and aeroelastic behavior and the pilot biomechanics, can be just as important and have recently received increasing research attention [4].

The major difference between the two kind of pilot-vehicle interaction resides in the participation of the pilot voluntary action. In the case of PIO, the deliberate action of the pilot on the aircraft controls is the principal source of the instability. In the case of PAO, it is instead the *involuntary* action of the pilot which is the major source of dynamic interaction. Pilots, in fact, act on the control inceptors both voluntarily - e.g. to accomplish the current flight Mission Task Element (MTE) - and involuntarily, through the filtering characteristics dictated by the biomechanics of their bodies. As shown in Fig. 1, the forcing due to the aircraft accelerations, $A(t)$, is fed to both the control device and the pilot neuromuscular system. The total force applied at the grip of the control device, F_{CD}, then results as the sum of the feedthrough component due to the control device itself (i.e. its inertia) and the pilot impedance, i.e. the frequency-dependent relationship between the inceptor rotation $\delta(t)$ and the force applied by the pilot on the control inceptor. Thus, in the latter case, it is the biomechanical characteristics of the pilot body, and the control device dynamics, that play a major role in defining the boundaries and properties of the unwanted feedback loop [11–14]

Correlated to the aforementioned difference in the pilot participation is the fact that the two classes of phenomena *live* in different frequency domains: PIO events occur in the frequency band associated with flight mechanics i.e. $(0,1]$ Hz, while PAOs typical frequencies are associated with the aeroelastic behavior of the aircraft and the biomechanical behavior of the human body, i.e. typically in the frequency range $(1,7]$ Hz.

Effort is needed to develop a comprehensive approach to rotorcraft design for RPC avoidance. The numerical modeling, particularly following the multibody approach, of the aircraft vibratory dynamics and the pilot upper body has been the focus of this research group in the past several years [9, 15] , with the goal of enabling a-priori evaluation of RPC proneness of rotorcraft during the design process. The focus on numerical modeling has been flanked, in the

Presented at the 48th European Rotorcraft Forum, Winterthur, Switzerland, 6-8 September, 2022

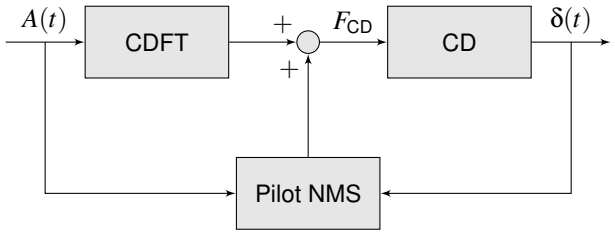

Figure 1: Block diagram of the pilot-control device system highlighting the feedback path responsible for the involuntary feedthrough of the forcing due to the cockpit accelerations, $A(t)$, to the control inceptor rotation $\delta(t)$, through the pilot neuro-muscular system (NMS) and the control device feedthrough (CDFT)

past two years and with the support of Leonardo Helicopter Division, by the development of a dedicated test-bed, able to support the validation of numerical models, to identify the BDFT of the pilot-rotorcraft system and the NMA of the pilot and to eventually enable the investigation of nonlinear effects, especially regarding the triggering of potential PAO interactions [15, 16].

In this view, a test-bed dedicated to the experimental investigation of rotorcraft-pilot couplings phenomena has been designed and assembled at Politecnico di Milano's Department of Aerospace Science and Technology facilities. It allows the analysis of the interactional dynamics of rotorcraft-pilot systems in controlled laboratory conditions by varying the parameters affecting the coupling. The approach to the identification of the pilot-rotorcraft BDFT will be the focus of the present work.

2 Research goals

The research project in which the experimental activity is included, named RPC (Rotorcraft Pilot Couplings) is focusing on proving tools for the robust design of the next generation rotorcraft, with respect to PAO proneness. The overall goals of the project can be summarized in the following major focus points:

1. enabling the experimental identification of pilot-rotorcraft systems' coupling indices, represented in the linear domain by the biodynamic feedthrough (BDFT) and the neuromuscular admittance (NMA);
2. develop a deep understanding of the dependence of said indices by influencing parameters;
3. exploit the analysis of experimental data to validate and develop detailed multibody models of the pilot biomechanics [9];
4. analyze the influence of nonlinear effects on the insurgence and sustenance of PAO events;
5. synthesize the experimental and numerical analyses results into design recommendations for robust design of novel rotorcraft.

The project is currently focusing on the first aspect, i.e. in providing reliable experimental data on pilot-rotorcraft involuntary interaction in a controlled laboratory setting. The first major focus has been placed on the measurement and identification of the BDFT, defined as the transfer function between the inceptor rotation $\delta(s)$ and the airframe acceleration input $A(s)$, evaluated at the cockpit floor or directly at the pilot seat:

$$H_{\text{BDFT}}(s) = \frac{\delta(s)}{A(s)} \tag{1}$$

The BDFT is a function of several different parameters, involving both the pilot biomechanics and the rotorcraft:

1. the pilot anthropometrics (age, height, weight, sex);
2. the pilot's muscular activation, and its dynamics;
3. the piloting task and the related cognitive workload;
4. the cockpit and control inceptors layout;
5. the control chain mechanical properties (inertia, trim/balancing elastic elements, friction...)

The required testing hardware and procedures must therefore be able to not only introduce the adequate forcing to excite the pilot-rotorcraft dynamics, but must also allow the reconfiguration of the cockpit layout, the modulation of the pilot task (and the associated workload) and the modification of the control chain in terms of inceptors' mass, retaining elements properties, and amount of friction.

3 Experimental Test-bed

An experimental test-bed (Cf. Figure 2) has been realized at the Department of Aerospace Science and Technology of Politecnico di Milano, to cope with the identified requirements. It is composed of the following subsystems:

1. a 6-DOF Motion Platform System (MPS) Bosch eMotion 1500;
2. a reconfigurable cockpit mock-up;
3. a customized measurement system.

The MPS is able to carry a maximum payload of $1500\,\text{kg}$ and provides acceleration inputs of adequate intensity (in excess of $10\,\text{m}\,\text{s}^{-2}$) in the frequency band of interest $[1, 7.5]$ Hz. The cockpit mock-up is composed of the pilot seat, collective and cyclic inceptors, pedals, and a glass cockpit made of two touchscreen monitors. The cockpit structures are supported by stainless steel frame. The data acquisition system is able to manage up to 40 channels. Currently, 9 accelerometers are attached to the MPS: 3 to the seat and 3 to each inceptor's grip. The rotation of the inceptors is measured by 3 absolute encoders. Furthermore, in the collective and cyclic grip, optical force sensors, purposely developed and based on frustrated total internal reflection of light [17, 18], are embedded.

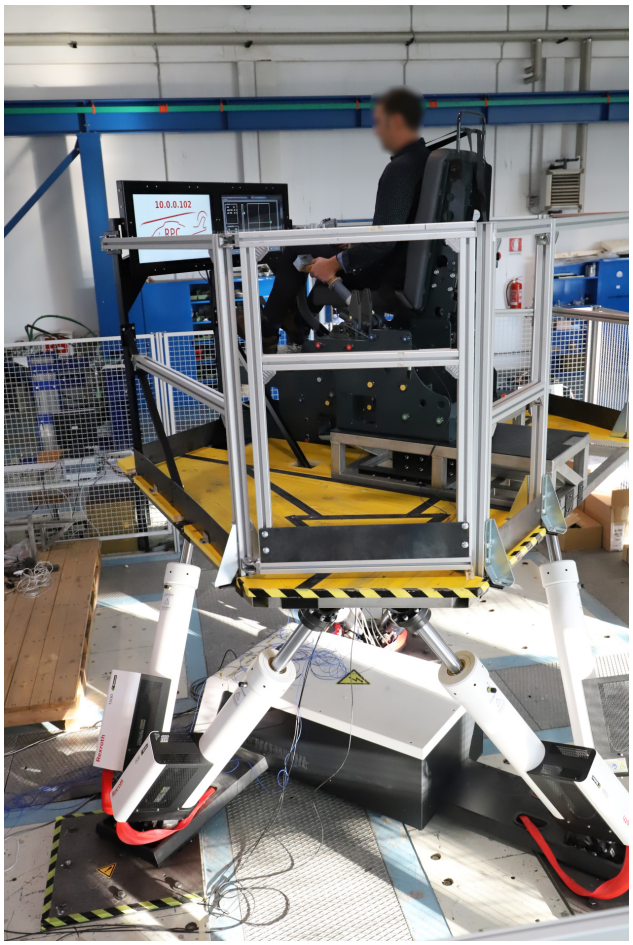

Figure 2: The RPC test-bed.

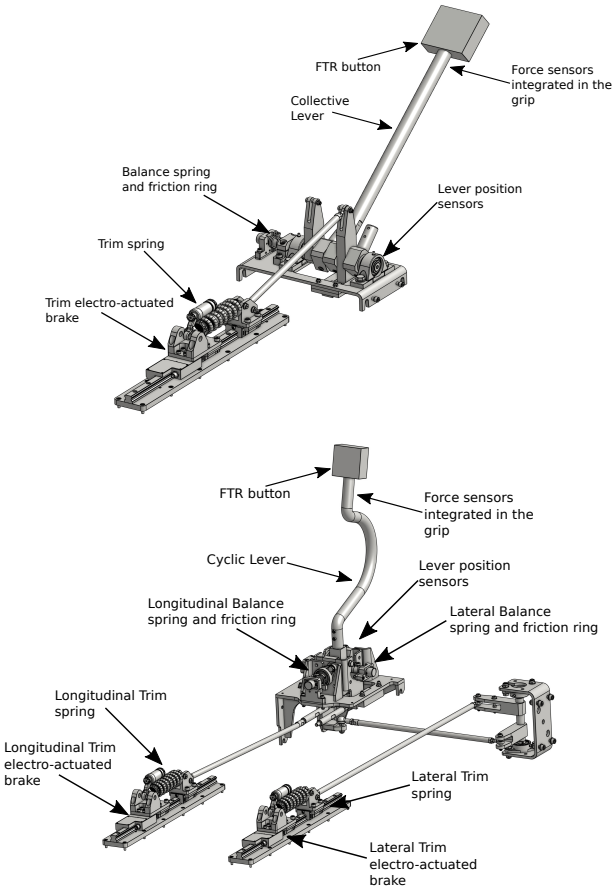

Figure 3: Fully mechanical passive model of the test-bed's collective and cyclic control chain.

The majority of the actual certified helicopters fly with a full mechanical control chain, linked directly to the actuators, eliminating the need for a synthetic force feel system to return a force feedback to the pilot, allowing the reproduction of this behavior without an active control loading system. Nevertheless, the mechanical characteristics of the inceptors and the feeling to the pilot are of primary importance. The test-bed control chain is specifically designed to reproduce the effect of all the components of the control chain as per a real rotorcraft without any augmentation system, a complete description may be found in [16]. A peculiar characteristic of the RPC test-bed is the capability of reproducing different cockpit layouts maintaining the correct geometry of the inceptors, the relative position of the pivot point with respect to the Seat Reference Point, and the mechanical characteristics of the levers. The collective and cyclic systems are sketched in Fig. 3: the relevant rotation is guaranteed by a torque tube equipped with a rotational balancing spring and an adjustable friction ring. The system is also predisposed to have a Force Trim, an electro-actuated brake, activated by a push-button on the grip, which can block a slider equipped with a linear spring, to add stiffness to the whole chain around the trim position. A typical inceptor force-displacement curve is sketched in Fig. 4 in trim OFF, blue, and trim ON, orange, condition.

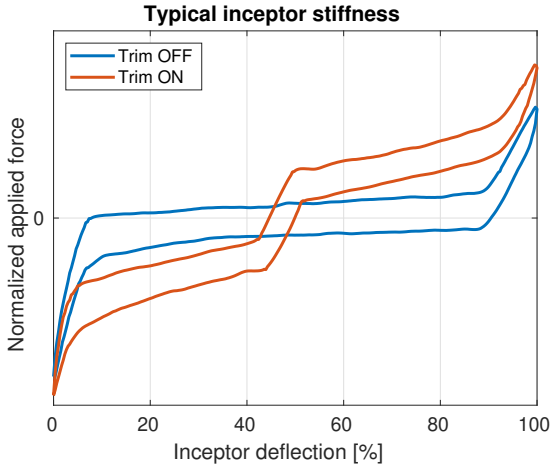

Figure 4: Constitutive law of the control inceptors springs, in trim OFF (blue) and trim ON (orange) condition.

3.1 Experimental tests design

During BDFT identification tests, the human-machine system is excited by prescribing the cockpit translational acceleration in the three directions X, Y, Z. The input signal is represented by a pseudo-random waveform obtained from the time realization of a flat Power Spectral Density (PSD) in the frequency band $[1, 7.5]$ hertz (Cf. Fig. 6). The frequency resolution of the time realization was set at $df = 0.1\,\mathrm{Hz}$. Each spectral line contribution to the time signal was gen-

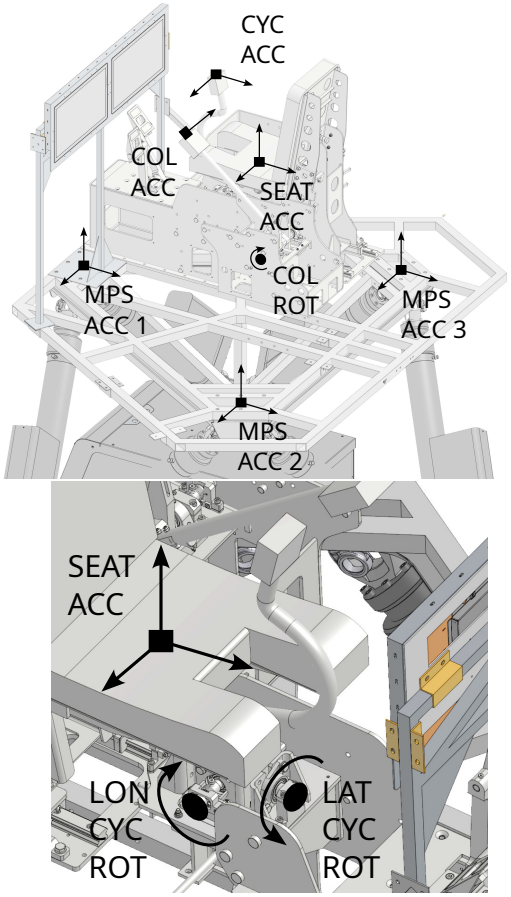

Figure 5: Schematics of the main sensors positions on the RPC test-bed: 9 accelerometers, represented by squares with arrows indicating their measurement directions, are placed on the MPS frame, for an accurate and complete measurement of the input acceleration. Two accelerometers are placed on the cyclic control grip and one on the collective control grip, in the tangential directions. Three more accelerometers are placed under the pilot seat. Rotation sensors (absolute encoders) measure the collective stick (picture above) and the cyclic stick (picture below) rotations.

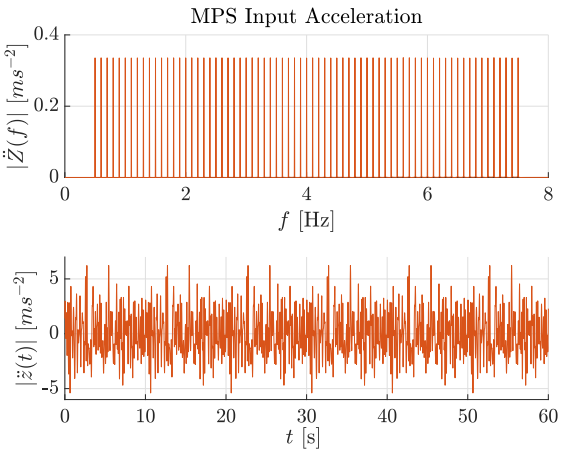

Figure 6: MPS acceleration input signal used in the BDFT identification tests. The pseudo-random input has been generated from the flat PSD shown in the graph at the figure top. The resulting time signal is shown in the graph at the bottom of the figure.

erated as a sine signal, with random phase:

$$a_i(t) = \sqrt{\frac{\mathrm{PSD}(f_i)df}{2}}\sin(2\pi f_i t + \varphi_i) \tag{2}$$

where $\mathrm{PSD}(f_i)$ is the value of the PSD at frequency f_i, and φ_i is a random phase between 0 and 2π. The value of the PSD has been set to reach the desired RMS acceleration level, i.e.

$$a_{\mathrm{RMS}} = \int_{f_1}^{f_2} \mathrm{PSD}(f)df \tag{3}$$

In the present case, $f_1 = 0.5\,\mathrm{Hz}$ and $f_2 = 7.5\,\mathrm{Hz}$. Tests were performed with single-axis input and multi-axis output. The input-output combination tested and analyzed in this work were the following:

- vertical acceleration input $\ddot{z}(t)$ and collective rotation $\delta(t)$ output;
- lateral acceleration input $\ddot{y}(t)$ and lateral cyclic rotation $\phi(t)$ output;
- longitudinal acceleration input $\ddot{x}(t)$ and longitudinal cyclic rotation $\psi(t)$ output;

The input accelerations RMS values were selected in order to ensure that the input-output coherence of the experimental frequency response functions (FRF)s were sufficiently close to 1.0 across the frequency band of the input. The resulting values are $1\,\mathrm{m\,s^{-2}}$ for the vertical axis acceleration $\ddot{z}(t)$, $0.5\,\mathrm{m\,s^{-2}}$ for the lateral axis acceleration $\ddot{y}(t)$ and $1.5\,\mathrm{m\,s^{-2}}$ for the longitudinal axis acceleration $\ddot{x}(t)$.

A professional test pilot was involved in the experimental campaign. The pilot was asked to perform simple tracking tasks (Cf. Fig. 7), keeping as much as possible the command input into the optimal $\pm 3\,\%$ range with respect to reference values. An error of $\pm 5\,\%$ was considered acceptable. Feedback was given to the pilot by changing the color of the marker indicating the current control input: a green marker indicated that the control input was in the optimal range, a yellow marker signaled that the control input was in the acceptable range and a red marker indicated that the current control input was outside the range of acceptance, i.e. that the absolute error between the desired and current control input was greater than $5\,\%$.

The duration of each test run was set at $60\,\mathrm{s}$. For each run, the target control input was set using an harmonic motion of constant amplitude and random phase. The mean of the signal was set at the reference collective and cyclic input of interest, which were varied in the test runs in order to explore the variability of the BDFT across the inceptor rotation range. The experimental approach followed best-practices identified in previous efforts [19, 20].

4 Data processing

Acquired waveforms of the inceptors rotation and of the base and seat accelerations were first bandpass filtered using a double-pass filtering algorithm, to avoid phase distortion, in the same frequency band of the input. The BDFT frequency response functions have been then calculated using the $H_v(j\omega)$ estimator:

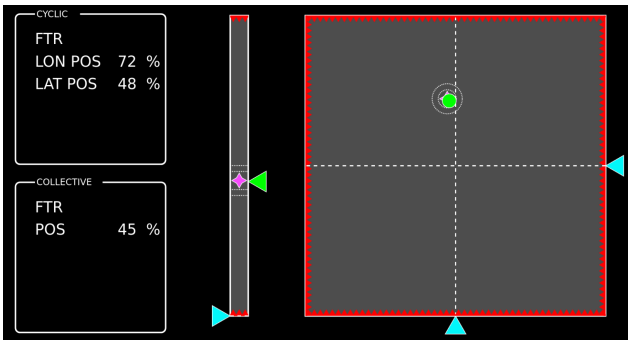

Figure 7: During BDFT identification tests, the pilot was asked to perform simple tracking tasks on an instrument mockup like the one depicted. The magenta diamonds indicate the desired control input. The dashed lines mark the optimal $\pm 3\,\%$ range and the acceptable $\pm 5\,\%$ range. The colored circle (cyclic input) and triangle (collective input) indicate the current control inputs - green when in the optimal range, yellow if outside the optimal and inside the acceptable range and red when outside of the acceptable range.

$$H_{\mathrm{BDFT}}(j\omega) = \left(H_1(j\omega)H_2(j\omega)\right)^{1/2} \tag{4}$$

where the H_1 and H_2 estimators are defined as

$$\begin{aligned} H_1 &= \frac{S_{\theta A}(j\omega)}{S_{AA}(j\omega)} \\ H_2 &= \frac{S_{\theta\theta}(j\omega)}{S_{A\theta}(j\omega)} \end{aligned} \tag{5}$$

where $S_{\theta A}(j\omega)$ is the cross-spectrum of the output inceptor rotation with respect to the input acceleration, and $S_{AA}(j\omega)$ is the auto-spectrum of the input MPS acceleration. Spectra were calculated using the Welch method on $10\,\mathrm{s}$ windows, overlapping by half of the window width.

Experimental frequency response functions were then fitted with a third order model having the following structure

$$H_{BDFT}(s) = \frac{(1+T_z s)}{(1+T_p s)} \cdot \frac{\mu e^{-\tau s}}{(s^2/\omega_n^2) + 2\zeta s/\omega_n + 1} \tag{6}$$

in which the dominant biomechanical complex conjugate poles are found at frequency ω_n and damping ζ_n, while the active low frequency behavior of the pilot is represented by the self canceling pole/zero pair (T_s, T_z) and a pure time delay of magnitude τ, which is also (optionally) introduced. The actual physical meaning of this term is closely related to a reaction time, representing the data processing lags in the central nervous system [21]. Its introduction is generally beneficial for the quality of the fitting, especially of the experimental FRFs phase. The static gain of the transfer function is μ.

5 Experimental results

The capabilities of the test-bed were evaluated in a preliminary test campaign performed by a professional test pilot. The test-bed was configured with a standard helicopter control inceptors setup, with a collective and a cyclic stick (and pedals, which however were not involved in the tests presented in this work). Two very different collective control sticks were tested: a *short* and *light* version, and a *long* and *heavy* version (Cf. Table 1). The dummy sticks were manufactured and tuned to represent the inertial properties of both the pilot and copilot control sticks. The pilot was

Property	units	value
Collective 1		
Mass	kg	1.21
Length	mm	350
CG Offset	mm	308
Moment of Inertia	$\mathrm{kg\,m^2}$	0.1352
Travel (at grip)	mm	110
Collective 2		
Mass	kg	3.35
Length	mm	800
CG Offset	mm	555
Moment of Inertia	$\mathrm{kg\,m^2}$	1.5245
Travel (at grip)	mm	110
Cyclic		
Mass	kg	2.71
Length	mm	550
CG Offset	mm	407
Lat M. of Inertia	$\mathrm{kg\,m^2}$	0.5545
Lon M. of Inertia	$\mathrm{kg\,m^2}$	0.5838
Lat Travel (at grip)	mm	110
Lon Travel (at grip)	mm	110

Table 1: Properties of the control sticks used during the BDFT identification test campaign. Lengths are referred to the distance between the pivot axis and the center of the grip. Moments of inertia and CG offsets are referred to the pivot axis.

asked to track the reference collective and cyclic references simultaneously during $60\,\mathrm{s}$ test runs. The complete test matrix is shown in Tab. 2. Each test case was repeated three times, for a total of 51 runs. Examples of the measured frequency response functions for the longitudinal acceleration input to longitudinal cyclic output case, and for the lateral acceleration input to lateral cyclic output case are shown in Figures 8 and 9. In Fig. 8, an example of the effect of the pure time delay is also represented. In this case, the value of the identified τ is $0.0273\,\mathrm{s}$. The fittings of the transfer functions, with the structure defined by eq. 6, are superimposed.

Values shown in the figures are normalized with respect to $\Delta\theta_0$, i.e. the collective lever absolute inclination with respect to the horizontal, in the static equilibrium conditions

Case	Input	COL [%]	LON CYC [%]	LAT CYC [%]
1	$\ddot{Z}$	10	50	50
2	$\ddot{Z}$	20	50	50
3	$\ddot{Z}$	50	50	50
4	$\ddot{Z}$	80	50	50
5	$\ddot{Z}$	90	50	50
6	$\ddot{Y}$	50	25	25
7	$\ddot{Y}$	50	25	50
8	$\ddot{Y}$	50	25	75
9	$\ddot{Y}$	50	50	25
10	$\ddot{Y}$	50	50	50
11	$\ddot{Y}$	50	50	75
12	$\ddot{Y}$	50	75	25
13	$\ddot{Y}$	50	75	50
14	$\ddot{Y}$	50	75	75
15	$\ddot{X}$	50	25	50
16	$\ddot{X}$	50	50	50
17	$\ddot{X}$	50	75	50
18	$\ddot{X}$	50	75	50
19	$\ddot{X}$	50	75	50
17	$\ddot{X}$	50	75	50

Table 2: Test matrix for the BDFT identification test campaign. Each test case was repeated three times, for a total of 51 test runs.

(i.e. at $50\,\%$ of the nominal range):

$$H_{\mathrm{BDFT}}(j\omega) = \frac{1}{\Delta\theta_0} \cdot \frac{S_{\theta,A}(j\omega)}{S_{AA}(j\omega)} \tag{7}$$

Trends of the identified frequencies $f_n = \omega_n/2/\pi$ and damping ratios ζ_n are shown in Figures 10 and 11. In the lateral direction, both frequencies and damping ratios are approximately constant across the command input range. The natural frequencies show a limited dispersion across the test runs, while the dispersion associated with the damping ratios increases towards reference positions associated with greater command input. In the longitudinal case, the natural frequency shows a drop at the $25\,\%$ reference position, with respect to the $50\,\%$ and $75\,\%$. The dispersion of the natural frequencies increases with the reference position. The damping ratios are instead almost constant with respect to the reference command position and show a small amount of dispersion across the runs.

An example of the experimental frequency response functions and associated fitted transfer functions for tests with vertical axis input, collective rotation output is shown in Fig. 12. The collective stick in this case is the shortest and lightest ("Colletive 1" of Table 1). A clear trend is visible in the natural frequency, which is significantly affected by the contribution of the control inceptor weight gradient with respect to the control deflection. The damping ratio is approximately stable with respect to the control deflection. Both the frequency and the damping ratio identified values show a significant amount of dispersion across the test runs.

The experimental frequency response functions and fitted transfer functions of test case 3, with the long and heavy

control stick configuration (Collective 2 of Tab 1 are shown in Figure 14). The identified natural frequencies and damping ratios, for the different collective reference deflections, are represented in Figure 15. An evident trend can be noted in the natural frequency, as was the case with the Collective 1 stick. The magnitude of the change in frequency is however less pronounced with respect to the Collective 2 stick case. The damping ratio is also approximately constant across the control stick deflection, as in the previous case.

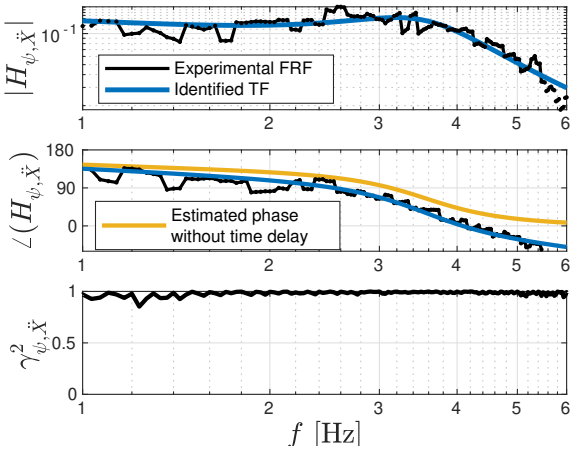

Figure 8: Experimental FRF and identified TF, test case 16 (Cf. Tab. 2): longitudinal acceleration input $\ddot{X}$, longitudinal cyclic rotation output ψ. Amplitude (top), phase [deg] (mid) with and without time delay, coherence (bottom). The input RMS is $1.5\,\mathrm{m\,s^{-2}}$.

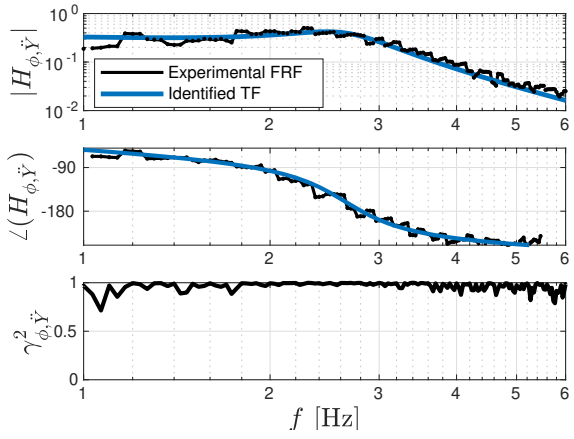

Figure 9: Experimental FRF and identified TF, test case 10 (Cf. Tab. 2): lateral acceleration input $\ddot{Y}$, lateral cyclic rotation output ϕ. Amplitude (top), phase [deg] (mid), coherence (bottom). The input RMS is $0.5\,\mathrm{m\,s^{-2}}$.

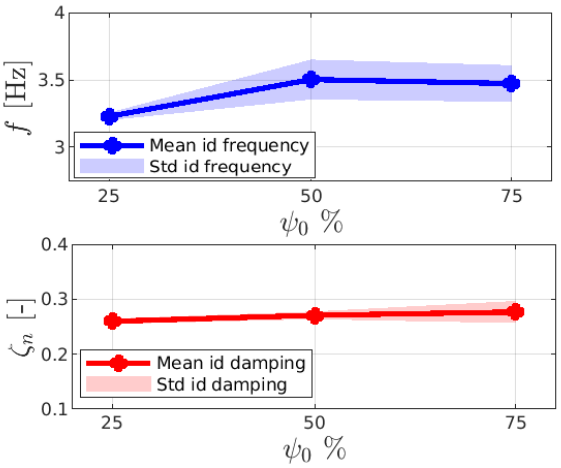

Figure 10: Mean and standard deviation of the identified frequency and damping at different longitudinal cyclic lever position. Input: longitudinal acceleration. Output: longitudinal cyclic rotation.

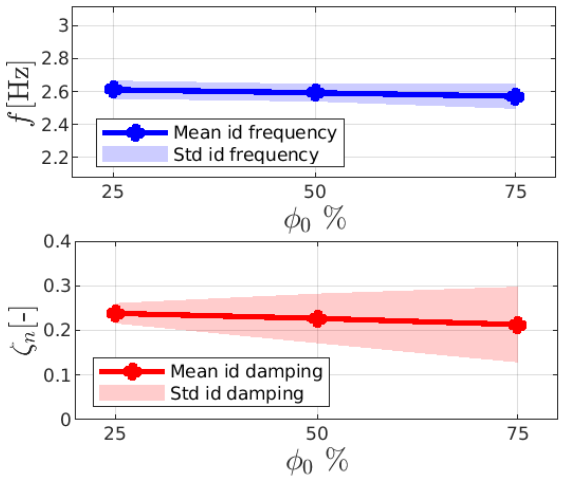

Figure 11: Mean and standard deviation of the identified frequency and damping at different lateral cyclic lever position. Input: lateral acceleration. Output: lateral cyclic rotation.

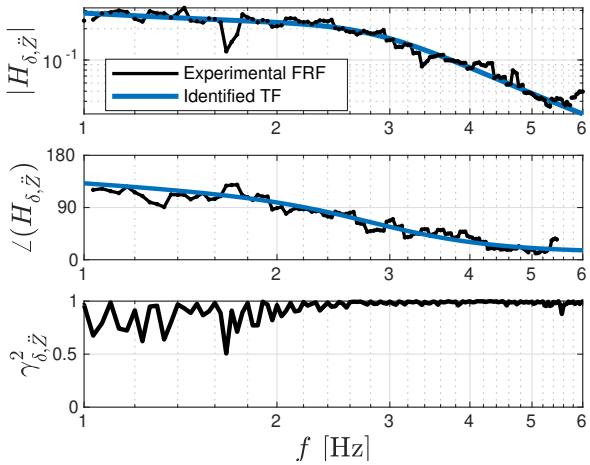

Figure 12: Experimental FRF and identified TF for test case 3 (Cf. Table 2). Input: vertical seat acceleration $\ddot{Z}$, collective rotation output δ. Amplitude (top), phase [deg] (mid), coherence (bottom). Input RMS $1\,\mathrm{m\,s^{-2}}$.

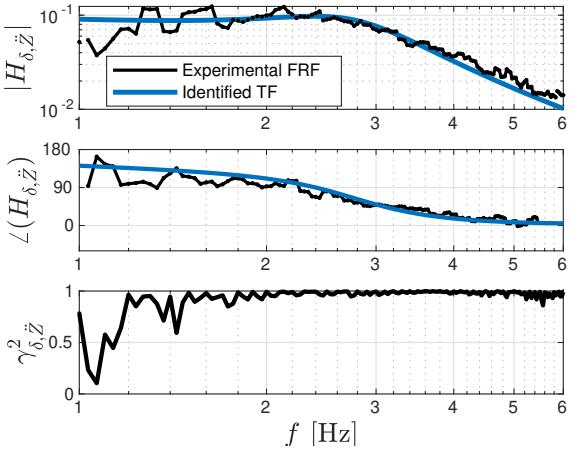

Figure 14: Experimental FRF and identified TF ,test case 2: vertical acceleration input $\ddot{Z}$ collective rotation output δ. Amplitude (top), phase [deg] (mid), coherence (bottom). The input RMS is $1.0\,\mathrm{m\,s^{-2}}$

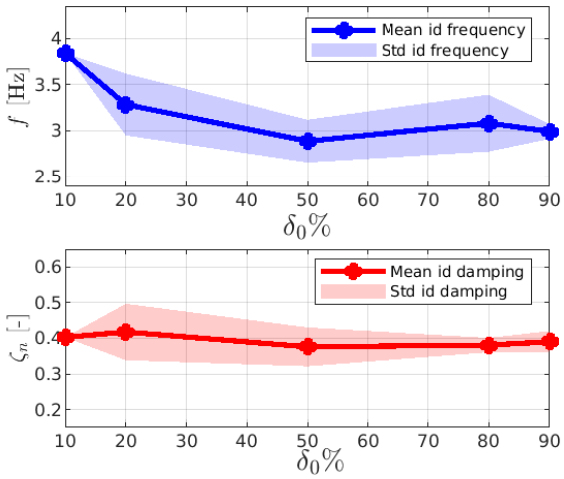

Figure 13: Mean and standard deviation of the identified frequency and damping at different collective lever position, short collective stick (Collective 1 of Table 1). Input: vertical acceleration $\ddot{Z}$. Output: collective rotation δ.

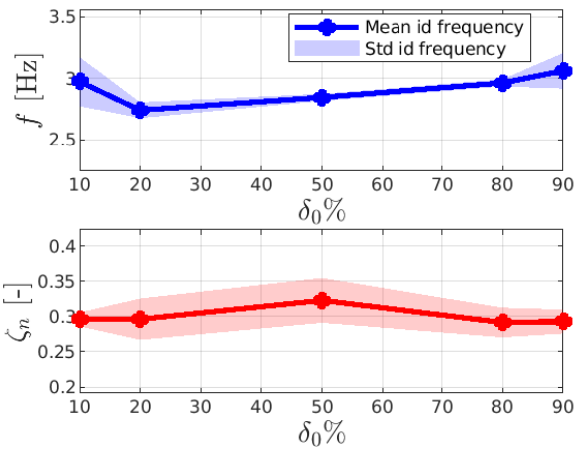

Figure 15: Mean and standard deviation of the identified frequency and damping at different collective lever position, long collective stick (Collective 2 of Table 1). Input: vertical acceleration $\ddot{Z}$. Output: collective rotation δ.

6 Collective bounce stability

The identified BDFT functions are exploited to perform a closed loop stability analysis for the coupled rotorcraft-pilot system. An example of how such an analysis can be performed is given in this section, considering the heave dynamics, with respect to the collective bounce phenomenon.

The input-output relationship between the airframe vertical acceleration, fed through the pilot biomechanics to the collective rotation, represented by the identified TFs, is used to realize a state-space representation through a standard canonical form. The state space system is coupled with a linear time invariant (LTI) representation of the helicopter rigid heave dynamics, augmented with the first collective flap dynamics (i.e. the main rotor coning mode) [7]. The closed loop system can be represented by the block scheme of Figure 16. The vertical acceleration of the airframe $\ddot{Z}$ is fed through the pilot biomechanics to the collective control deflection, which in turn produced a vertical acceleration of the airframe, through the combined effect of the rigid heave mode and the rotor coning mode. The loop transfer function of the pilot-vehicle system can be written as follows:

$$H_{\text{PVS}}(s) = -GH_{\text{BDFT}}(s)H_{\ddot{Z}\delta}(s) \tag{8}$$

where G is the gear ratio relating the collective control stick deflection and the collective blade pitch, and $H_{\ddot{Z}\delta}(s)$ is the

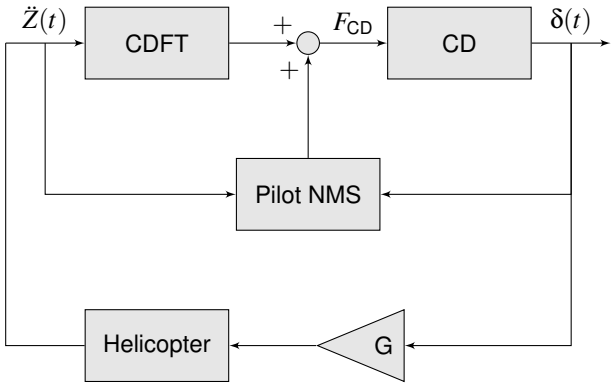

Figure 16: Block diagram of the pilot-helicopter close loop system for heave dynamics.

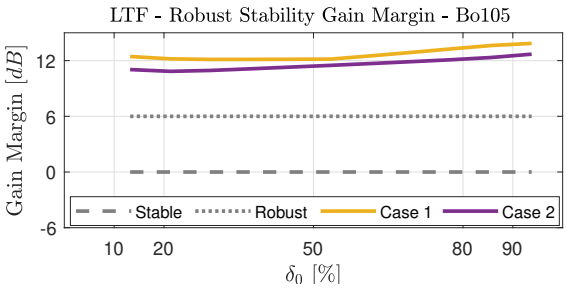

Figure 17: Gain margin for the closed loop stability of collective bounce, Bo105 parameters of Table 3, with collective 1 and 2 of Table 1.

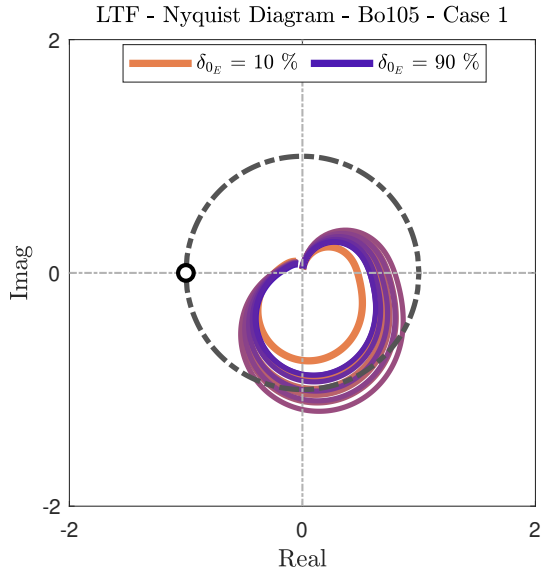

(a)

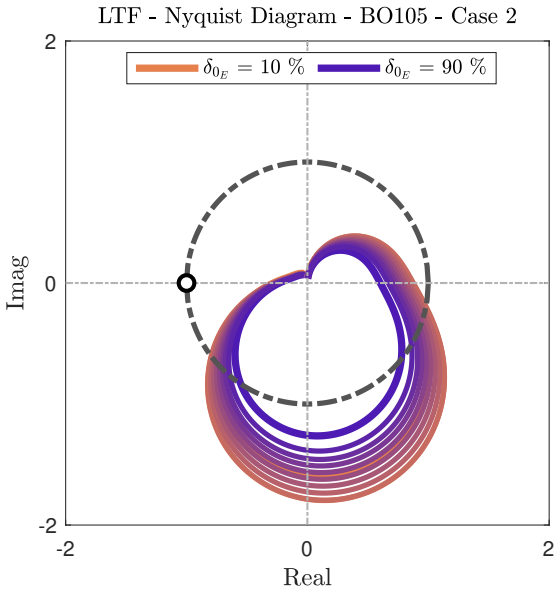

(b)

Figure 18: Nyquist diagram of the closed loop stability of collective bounce. The Bo105 helicopter model parameters of Table 3 are employed. Figure (a) shows the results obtained with collective stick 1 of Table 1. Figure (b) refer to results obtained with collective stick 2 of Table 1.

Parameter	Symbol	Units	Value (Bo105)	Value (CH53)
Number of blades	N_b	-	4	6
Mass	M	kg	2055	10750
Rotor Radius	R	m	4.90	11.01
Rotor Speed	Ω	Hz	7.07	3.07
Lock Number	γ	-	4.31	12.40
Blade mass	m	kg	50.61	135.84
Flap static mom.	S_b	$\mathrm{kg\,m^{-1}}$	80.17	819
Flap inertia mom.	I_b	$\mathrm{kg\,m^{-1}}$	249.85	5489
Flap freq. ratio	ν_β	-	1.076	1.048
Coning damping	ξ_β	-	0.25	0.74
Gear Ratio (1)	G_1	-	0.52	0.68
Gear Ratio (2)	G_2	-	1.02	1.35

Table 3: Parameters for the 2 d.o.f. model of the helicopter heave dynamics, for the Bo105 and the CH53. Different data sources [22, 23] were exploited, along with some basic estimation of missing properties.

transfer function between the collective pitch and the vertical acceleration, derived from the LTI model analysis (the equations of motion of the helicopter heave dynamics model and the full derivation of the coupling process can be found in [7]). The stability margin of the closed-loop system has been evaluated using two different sets of parameters for the helicopter model. The first set is representative of a Bo105 helicopter, while the second one is derived from available data of the CH53. The values of the model parameters are shown in Table 3. The gain margin of the system's closed loop transfer function has been selected as the metric associated with the system stability. The gain margin is defined as the inverse of the system's closed loop transfer function, when its phase crosses $-180°$:

$$G_m = \frac{1}{H_{\mathrm{LTF}}(j\omega_{-180})} \tag{9}$$

Typically, values of G_m above $6\,\mathrm{dB}$ indicates robust stability,

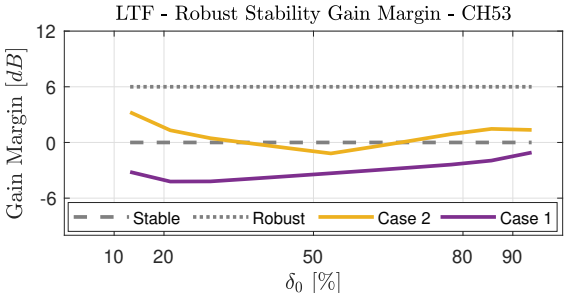

Figure 19: Gain margin for the closed loop stability of collective bounce, CH53 parameters of Table 3, obtained with collective sticks 1 and 2 of Table 1.

while negative values indicate that the system is unstable. Each of the two different helicopter models was coupled with both BDFTs identified using the two different collective control sticks of Table 1, to highlight the modifications introduced by the different control layout and inertia properties to the overall stability to collective bounce.

Gain margins of the pilot-helicopter closed loop transfer function obtained considering the Bo105 parameters are shown in Figure 17. The system is stable and robust with wide margins, with both the collective stick assemblies considered. A reduction of the stability margin is however noticeable when the longer and heavier collective lever ("Collective 2" of Table 1) is employed, with respect to the shortest and lighter alternative ("Collective 1" of Table 1). The same pattern can be observed in the CH53 case, reported in Figure 19. In this case, the characteristics of the helicopter make it more prone to collective bounce in general (a result that was found and explained in detail in [7]): in fact, for the vast majority of the collective range the closed-loop system is only marginally stable, when considering "Collective 1" characteristics. In the proximity of the $50\,\%$ input, it even becomes unstable. In accordance to what is observed for the Bo105, a significant reduction in the stability margin is found when employing "Collective 2". The reduction in the stability margin is probably due to a combination of effects: e.g., a longer inceptor is generally associated with increased static moment, which contributes to the inertial forcing of the collective dynamics. Furthermore, a longer lever is associated with a shorter angular travel, since the linear travel of the pilot hand is generally fixed due to ergonomics. A shorter angular range, in turn, results in a larger gear ratio between the collective stick rotation and the change in blade pitch, augmenting the LTF static gain. The effect is particularly evident in the Nyquist plots, shown in Figures 18 and 20. In particular, one can notice that the effects associated with changing the collective lever parameters are more pronounced than one is led to believe just considering the gain margin evolution. The overall area enclosed by the LTF curve increases significantly moving from "Collective 1" to "Collective 2", and also the slope of the LTF at the intersection with the real axis - associated with another measure of the system stability, the phase margin - increases noticeably. In the Bo105 case, this is not sufficient to erode the initial advantage too much, but it can be noticed nonetheless, again considering the slope of the LTF at the real axis intersection, that a dangerous condition is approaching for collective inputs close to $50\,\%$ in the case of "Collective 2" parameters.

7 Conclusions and future developments

An experimental testbed dedicated to the measurement of the biodynamic feedthrough of rotorcraft pilot-control systems, installed at Politecnico di Milano's Department of Aerospace Science and Technology premises, has been described. Initial results obtained during a test campaign involving a professional test pilot and two different collective stick control chain layouts are shown, confirming that the test bed is able to produce the expected identification results. The latter are then exploited, for the collective axis,

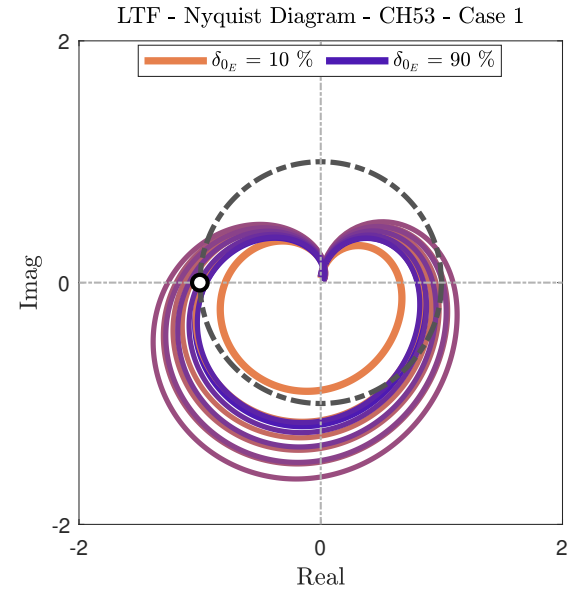

(a)

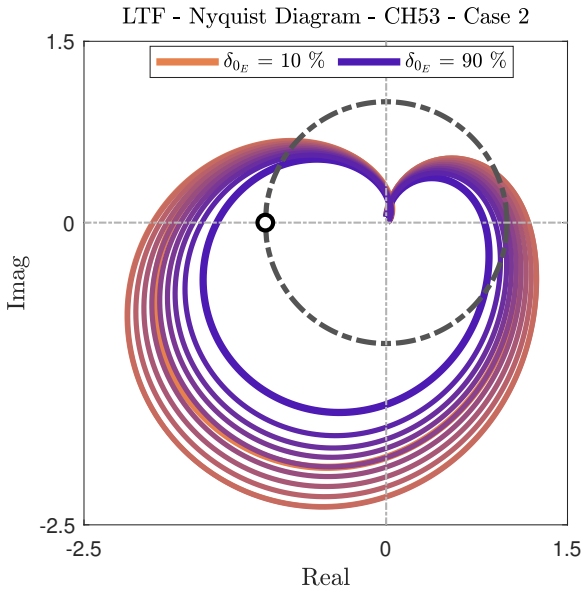

(b)

Figure 20: Nyquist diagram of the closed loop stability of collective bounce. The CH53 helicopter model parameters of Table 3 are employed. Figure (a) shows the results obtained with collective stick 1 of Table 1. Figure (b) shows to results obtained with collective stick 2 of Table 1.

in performing the closed-loop stability assessment with respect to collective bounce, following an established analysis both confirming previously published results and enhancing them with experimental validation, albeit partial.

In the near future, the experimental campaign will be extended to other control chain layouts and different pilots, with the goal of evaluating the sensitivity of the closed-loop stability margins from design parameters, on one side, and the robustness of the design choices with respect to the intrinsic variability of the human biomechanical response, on the other. The analysis will be also extended to the lateral and longitudinal axes, with the final goal of developing an encompassing set of tools and recommendations able to assist future engineers in designing RPC-free rotorcraft.

References

[1] Ashkenas, I. L., Jex, H. R., and McRuer, D. T., "Pilot-Induced Oscillations: Their Cause and Analysis," NCR 64-143, Norair Report, June 20 1964.

[2] McRuer, D. T., "Pilot-Induced Oscillations and Human Dynamic Behavior," CR 4683, NASA, 1995.

[3] McRuer, D. T., *Aviation Safety and Pilot Control: Understanding and Preventing Unfavourable Pilot-Vehicle Interactions*, Washington DC: National Research Council, National Academy Press, 1997.

[4] Pavel, M. D., Jump, M., Dang-Vu, B., Masarati, P., Gennaretti, M., Ionita, A., Zaichik, L., Smaili, H., Quaranta, G., Yilmaz, D., Jones, M., Serafini, J., and Malecki, J., "Adverse rotorcraft pilot couplings — Past, present and future challenges," *Progress in Aerospace Sciences*, Vol. 62, doi:10.1016/j.paerosci.2013.04.003, October 2013, pp. 1–51.

[5] Pavel, M. D., Masarati, P., Gennaretti, M., Jump, M., Zaichik, L., Dang-Vu, B., Lu, L., Yilmaz, D., Quaranta, G., Ionita, A., and Serafini, J., "Practices to identify and preclude adverse aircraft-and-rotorcraft pilot couplings — A design perspective," *Progress in Aerospace Sciences*, doi:10.1016/j.paerosci.2015.05.002, 2015.

[6] Pavel, M. D., Jump, M., Masarati, P., Zaichik, L., Dang-Vu, B., Smaili, H., Quaranta, G., Stroosma, O., Yilmaz, D., Jones, M., Gennaretti, M., and Ionita, A., "Practices to identify and prevent adverse aircraft-and-rotorcraft pilot couplings — A ground simulator perspective," *Progress in Aerospace Sciences*, doi:10.1016/j.paerosci.2015.06.007, 2015.

[7] Muscarello, V., Quaranta, G., and Masarati, P., "The Role of Rotor Coning in Helicopter Proneness to Collective Bounce," *Aerospace Science and Technology*, Vol. 36, doi:10.1016/j.ast.2014.04.006, July 2014, pp. 103–113.

[8] Muscarello, V., Colombo, F., Quaranta, G., and Masarati, P., "Aeroelastic rotorcraft–pilot couplings in tiltrotor aircraft," *Journal of Guidance, Control, and Dynamics*, Vol. 42, (3), 2019, pp. 524–537.

[9] Zanoni, A., Cocco, A., and Masarati, P., "Multibody dynamics analysis of the human upper body for rotorcraft–pilot interaction," *Nonlinear Dynamics*, Vol. 102, (3), doi:10.1007/s11071-020-06005-7, 2020, pp. 1517–1539.

[10] Olivari, M., Nieuwenhuizen, F. M., Venrooij, J., Bülthoff, H. H., and Pollini, L., "Methods for Multiloop Identification of Visual and Neuromuscular Pilot Responses," *IEEE Transactions on Cybernetics*, Vol. 45, (12), Conference Name: IEEE Transactions on Cybernetics, December 2015, pp. 2780–2791. doi: 10.1109/TCYB.2014.2384525

[11] Quaranta, G., Masarati, P., and Venrooij, J., "Impact of pilots' biodynamic feedthrough on rotorcraft by robust stability," *Journal of Sound and Vibration*, Vol. 332, (20), doi:10.1016/j.jsv.2013.04.020, September 2013, pp. 4948–4962.

[12] Venrooij, J., Abbink, D. A., Mulder, M., van Paassen, M. M., Mulder, M., van Helm, F. C. T. d., and Bulthoff, H. H., "A Biodynamic Feedthrough Model Based on Neuromuscular Principles," *IEEE Transactions on Cybernetics*, Vol. PP, (99), doi:10.1109/TCYB.2013.2280028, 2013, pp. 1–1.

[13] Venrooij, J., *Measuring, modeling and mitigating biodynamic feedthrough*, Ph.D. thesis, 2014.

[14] Zanoni, A., Zago, M., Paolini, R., Quaranta, G., Galli, E., and Masarati, P., "On task-dependence of helicopter pilot biodynamic feedthrough and neuromuscular admittance. An experimental and numerical study," *IEEE Transactions on Human-Machine Systems*, doi:10.1109/THMS.2020.3044971, available online Jan 2021.

[15] Zanoni, A., Cocco, A., and Masarati, P., "Numerical Investigation on the Role of Control Inceptors Layout in Rotorcraft-Pilot Couplings," 77th Forum of the Vertical Flight Society, May 11–13 2021.

[16] Zanoni, A., Cocco, A., Marchesoli, D., Talamo, C., Masarati, P., Colombo, F., Kemp, S., and Fosco, E., "Pilot Biomechanics for the Definition of a Rotorcraft-Pilot Interaction Experiment," 78th Forum of the Vertical Flight Society, May 20–22 2022.

[17] Zanoni, A., Garbo, P., and Quaranta, G., "Online evaluation of helicopter pilot workload during flight simulator experiments," AIAA SCITECH 2022 Forum. doi: 10.2514/6.2022-0511

[18] Zanoni, A., Garbo, P., Quaranta, G., and Lavatelli, A., "Optical Pressure Sensor," Patent Application PCT/IB2022/052048, 2022.

[19] Venrooij, J., Yilmaz, D., Pavel, M. D., Quaranta, G., Jump, M., and Mulder, M., "Measuring Biodynamic Feedthrough in Helicopters," 37th European Rotorcraft Forum, September 13–15 2011.

[20] Masarati, P., Quaranta, G., and Jump, M., "Experimental and Numerical Helicopter Pilot Characterization for Aeroelastic Rotorcraft-Pilot Couplings Analysis," *Proc. IMechE, Part G: J. Aerospace Engineering*, Vol. 227, (1), doi:10.1177/0954410011427662, January 2013, pp. 124–140.

[21] McRuer, D. T., "Human Pilot Dynamics in Compensatory Systems," AFFDL-TR 65-15, 1965.

[22] Padfield, G. D., *Helicopter Flight Dynamics: The Theory and Application of Flying Qualities and Simulation Modelling*, Blackwell Publishing, 2007.

[23] Sturgeon, W. R. and Phillips, J. D., "A Mathematical Model of the CH-53 Helicopter," TM 81238, NASA, 1980.